

# Energetics of drop deformation with application to turbulence

Alberto Vela-Martín<sup>1,2†</sup>, Marc Avila<sup>1</sup>

<sup>1</sup>Center of Applied Space Technology and Microgravity (ZARM) University of Bremen, 28359 Bremen

<sup>2</sup>School of Aeronautics, Universidad Politécnica de Madrid, 28040 Madrid, Spain

(Received xx; revised xx; accepted xx)

Drop deformation in fluid flows is investigated here as an exchange between the kinetic energy of the fluid and the surface energy of the drop. We show analytically that this energetic exchange is governed only by the action of the rate-of-strain tensor on the surface of the drop, more specifically, by a mechanism analogous to vortex stretching. Our formulation allows to isolate the energetic exchange due to drop-induced surface effects from the external action of turbulence fluctuations. We perform direct numerical simulations of single drops in isotropic homogeneous turbulence and show that an important contribution to the energetic exchange arises from the stretching of the fluid-fluid interface by velocity fluctuations far from the drop surface. The identification of this mechanism, which is approximately independent of surface dynamics in a wide range of Weber numbers, sheds new light on drop deformation in turbulent flows, and opens the venue for the improvement and simplification of breakup models.

**Key words:** turbulence, drop breakup, diffuse-interface methods

## 1. Introduction

The deformation of drops in turbulent flows is a key process in many natural phenomena and industrial applications. Understanding the physical mechanisms that drive this process is essential to develop accurate models to predict drop breakup (Hakansson 2019). Breakup models are necessary to predict the dynamics of binary mixtures and the distribution of drop sizes, a relevant problem initiated with the seminal work of Kolmogorov (1949) and Hinze (1955). Many commonly used models rely on an energetic description of drop deformation, in which the surface energy of the drop increases due to interactions with turbulent fluctuations until a maximum energy is reached and the drop breaks. In particular, a widespread phenomenological picture describes drop deformation and breakup as caused by the ‘impact’ of eddies on the surface of the drop (Andersson & Andersson 2006). The kinetic energy of these eddies and their arrival frequency are relevant model parameters, and an efficiency is usually introduced to account for an incomplete energetic exchange in the process (see e.g. Lasheras *et al.* 2002; Liao & Lucas 2009, for reviews). This approach to modeling breakup is convenient because it lumps the complexity of drop-turbulence interactions into model parameters, but it depends on the validity of the model assumptions about the energetic exchange between the drop and the turbulent flow.

† Email address for correspondence: albertovelam@gmail.com

Laboratory experiments to validate and to parametrise these (and other) models are extremely challenging (see e.g. Risso & Fabre 1998; Eastwood *et al.* 2004; Maaß & Kraume 2012), hindering accurate predictions of drop breakup and drop-size distributions even in simple turbulent flows (Aiyer *et al.* 2019). Direct numerical simulations have recently provided quality data to study the energetics of drop-turbulence interactions (Dodd & Ferrante 2016), but a poor understanding of the energy exchange mechanisms limits the exploitation of these results for modelling.

A convenient framework to analyze the energetic exchange between the kinetic energy of the fluids and the surface energy of a drop (or more precisely the free energy of the fluid mixture) is given by the Cahn–Hilliard–Navier–Stokes equations (Jacqmin 1999). In these equations the interface is of finite thickness  $\epsilon$ , but as  $\epsilon \rightarrow 0$  the sharp-interface limit is recovered (with the classical stress balance at the infinitesimal fluid–fluid interface, see Magaletti *et al.* 2013). In this paper, we exploit this framework to show that this energetic exchange is solely described by the action of the rate-of-strain tensor on the surface of the drop. Moreover, this formulation allows to distinguish the self-induced increments due to surface dynamics from the action of the surrounding turbulence. In this paper, we leverage this approach to shed light on the mechanisms of drop deformation and breakup in homogeneous isotropic turbulence.

This paper is organised as follows. In §2, we present the derivation of the fundamental mechanisms that drives the exchange between kinetic energy and surface energy. We study this mechanism in direct numerical simulations of single drops, which are described in §3. The results and their discussion are presented in §4 and §5. Finally, conclusions are offered in §6.

## 2. Exchange between kinetic energy and surface energy

We consider the incompressible Navier–Stokes (NS) equations coupled to the Cahn–Hilliard (CH) equations,

$$\begin{aligned}\rho(\partial_t u_i + u_j \partial_j u_i) &= -\partial_i \tilde{p} + 2\partial_j \mu S_{ij} + f_i - c\partial_i \phi, \\ \partial_t c + u_j \partial_j c &= \kappa \partial_{kk} \phi,\end{aligned}\tag{2.1}$$

which, together with the incompressibility constraint,  $\partial_i u_i = 0$ , describe the evolution of an immiscible binary mixture of incompressible fluids (Jacqmin 1999). Here  $u_i$  is the  $i$ -th component of the velocity vector,  $\tilde{p}$  is a modified pressure,  $S_{ij} = \frac{1}{2}(\partial_i u_j + \partial_j u_i)$  is the rate-of-strain tensor and  $f_i$  is a body-force term per unit volume. Repeated indices imply summation, and we consider periodic boundary conditions. The concentration of each component in the mixture is represented by  $c$ , where  $c = \pm 1$  are the pure components. The density,  $\rho$ , and the dynamic viscosity,  $\mu$ , of the fluid mixture depend on  $c$ , and the immiscibility is modeled through a chemical potential,

$$\phi = \beta(c^2 - 1)c - \alpha \partial_{kk} c.\tag{2.2}$$

The true pressure is related to the modified pressure by  $p = \tilde{p} + c\phi - \beta/4(c^2 - 1)^2 + \alpha/2(\partial_i c)^2$  (Jacqmin 1999). The action of interfacial forces in the momentum equation is represented by  $c\partial_i \phi$ , which is derived from physical energy-conservation arguments, and consistently reproduces the linear relation between surface tension forces and the local curvature of the interface (Jacqmin 1999). The numerical parameters  $\alpha$  and  $\beta$  determine the typical width of the fluid–fluid interface,  $\epsilon = 4\sqrt{2\alpha/\beta}$ , and the mobility,  $\kappa$ , determines its typical relaxation time. When these parameters are fixed appropriately,  $\kappa \sim \epsilon^2$  (Magaletti *et al.* 2013), the interface is consistently close to the equilibrium profile,  $c_{eq}(x) = \tanh(4x/\epsilon)$ ,

and the surface tension reads

$$\sigma = \alpha \int_{-\infty}^{+\infty} (\partial_i c_{eq})^2 dx = \frac{4}{3\sqrt{2}} \sqrt{\alpha\beta}, \quad (2.3)$$

where  $x$  is the spatial coordinate in the direction normal to the interface.

### 2.1. Governing equations of the kinetic energy and the surface energy

The evolution equation of the kinetic energy of the flow is obtained by taking the dot product of the NS equations with  $u_i$ . We consider that  $-c\partial_i\phi = \phi\partial_i c - \partial_i(c\phi)$ , and the second term in the right-hand side is absorbed into a new modified pressure,  $p' = \tilde{p} - c\phi$ . Then the equation reads

$$\partial_t e + u_j \partial_j e = \partial_i (u_i p' + 2\mu u_j S_{ij}) - 2\mu S_{ij} S_{ij} + u_i \phi \partial_i c + u_i f_i, \quad (2.4)$$

where  $e = 1/2 \rho u_i u_i$  is the turbulent kinetic energy per unit volume. Considering periodic boundary conditions, or in the absence of boundary fluxes, the only terms contributing on average to the total kinetic energy budget are the local kinetic energy dissipation,  $2\mu S_{ij} S_{ij}$ , the power input,  $u_i f_i$ , and the energetic exchange between the kinetic energy and the surface energy,  $\phi u_i \partial_i c$ . By multiplying the CH equation by the chemical potential, we obtain,

$$\partial_t h + u_j \phi \partial_j c = \kappa \phi \partial_{kk} \phi, \quad (2.5)$$

where  $h = \beta/4(c^2 - 1)^2 + \alpha/2(\partial_k c)^2$  is the free energy per unit volume. We now transform (2.5) into an advection equation for  $h$  by decomposing the product  $\phi \partial_i c$  and operating on the partial derivatives. We find the relation

$$\phi \partial_i c = \partial_i h - \alpha \partial_k \tau_{ik}, \quad (2.6)$$

where  $\tau_{ik} = \partial_i c \partial_k c$  is a Korteweg stress tensor. Substituting this expression in the kinetic energy equation and the free energy equation, we obtain

$$\begin{aligned} \partial_t e + u_j \partial_j e &= \partial_i \Psi_i - 2\mu S_{ij} S_{ij} - \alpha u_i \partial_j \tau_{ij} + u_i f_i, \\ \partial_t h + u_j \partial_j h &= \kappa \phi \partial_{kk} \phi + \alpha u_i \partial_j \tau_{ij}, \end{aligned} \quad (2.7)$$

where  $\Psi_i = u_i(p' + h) + 2\mu u_j S_{ij}$ , and  $p' + h = p + \alpha(\partial_i c)^2$ . The free energy equation has been transformed into an advection equation, where the first term in the right-hand side represents the diffusive and dissipative action of the chemical potential, and the second term the interaction of the fluid-fluid interface with the velocity field. This term describes the action of a stress tensor,  $\tau_{ij}$ , and also appears in the kinetic energy equation.

### 2.2. The physical mechanism of the surface energy variations

The energy-exchange term can be further expanded into

$$\alpha u_i \partial_j \tau_{ij} = \alpha \partial_j (u_i \tau_{ij}) - \alpha S_{ij} \tau_{ij}. \quad (2.8)$$

The first term in the right-hand side represents the divergence of a flux and vanishes in the mean for closed surfaces away from solid boundaries. Furthermore due to the symmetric form of  $\tau_{ij}$ , only the symmetric part of the velocity gradient tensor, the rate-of-strain tensor  $S_{ij}$ , interacts with  $\tau_{ij}$ . Considering that the components of the vector normal to the interface are  $n_i = \partial_i c / \gamma$ , where  $\gamma = \sqrt{(\partial_k c)^2}$ , we rewrite the stress tensor as  $\tau_{ij} = -\alpha \gamma^2 n_i n_j$ , and the exchange term as  $-\alpha \gamma^2 n_i S_{ij} n_j$ . This term describes the change in free energy per unit volume; by integrating normal to the interface we transform it into an energy change per unit surface,

$$\vartheta = -\sigma n_i S_{ij} n_j. \quad (2.9)$$

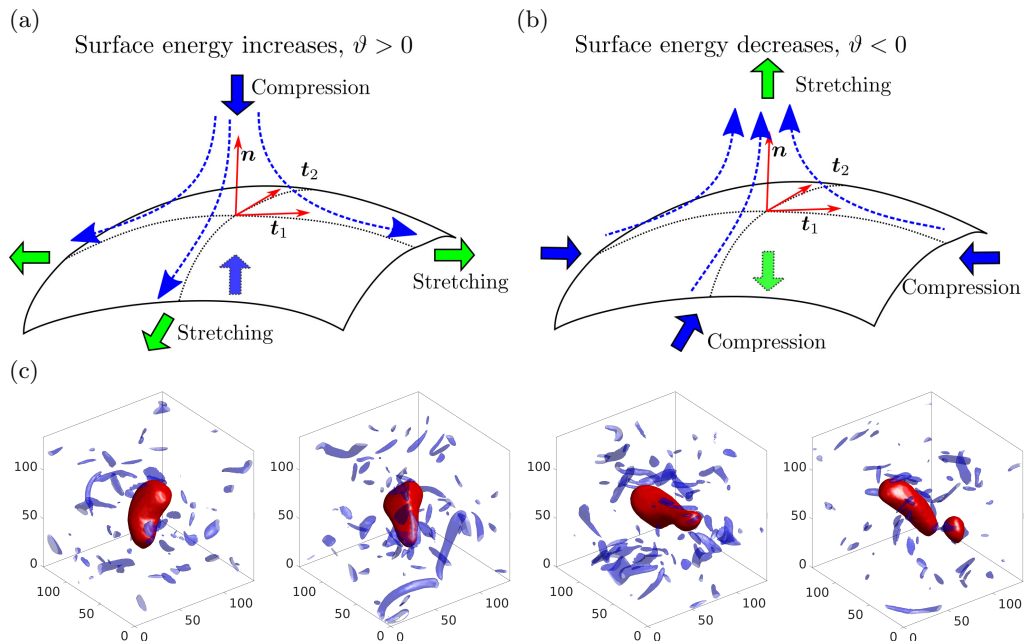


FIGURE 1. (a,b) Schematic representation of the mechanism that generates (a) positive and (b) negative increments of the surface energy due to the compression or stretching of the drop surface, where  $\mathbf{n}$  is the orthogonal vector normal to the interface,  $\mathbf{t}^1$  and  $\mathbf{t}^2$  are vectors parallel to the surface, and  $\vartheta = -\sigma n_i S_{ij} n_j$ . Blue and green arrows indicate the compressive and stretching directions of the rate-of-strain tensor at the surface, and dotted lines are the streamlines of the velocity field with respect to the surface. (c) Temporal evolution of a drop at  $We = 1.8$ . The frame is fixed at the center of the drop, and the time of the snapshots corresponds, from left to right, to  $t/t_d = 2.0, 2.9, 3.9, 4.8,$  and  $5.1$ . Blue isosurfaces denote vorticity with magnitude  $|\boldsymbol{\omega}| = 2.6\langle|\boldsymbol{\omega}|\rangle$ . The size of the computational box is marked in Kolmogorov units.

Here we have assumed that the interface is in equilibrium (so that eq. (2.3) holds) and that neither  $\mathbf{n}$  nor  $S_{ij}$  change substantially across the interface width. Both assumptions are fulfilled in the sharp-interface limit (Magaletti *et al.* 2013). The expression in (2.9) resembles the vortex stretching term in the evolution equation of the enstrophy (squared vorticity), which is responsible for the amplification of the vorticity vector. By analogy,  $\vartheta$  describes the stretching or contraction of the interface width by the rate-of-strain tensor. This result may be difficult to interpret from a physical and geometrical perspective, because the width of the interface between immiscible fluids is of molecular scale, and its relaxation time is much faster than the time-scale of the velocity gradients. In what follows, we give this term a physical interpretation.

For simplicity and consistency with the numerical simulations shown later in this paper, we have considered incompressible fluids. However the expression in (2.8), and the subsequent analysis, holds regardless of the divergence of the velocity field. We have only assumed that the gradients of the velocity field take place at a scale much larger than the interface thickness. The expression in (2.9) is also valid for compressible flows as long as the velocity field does not contain any discontinuity in the interface. Compressibility modifies the energy equations in (2.7), since new fluxes and extra variables appear (in particular the surface tension forcing terms added to the modified pressure must be considered separately), but does not modify the structure of the exchange term, which still remains the only net source of energy exchange. For the sake of generality we consider,

only in the following analysis, a compressible flow, and decompose the rate-of-strain tensor into a deviatoric and a volumetric part,  $S_{ij} = S_{ij}^d + P/3\delta_{ij}$ , where  $\delta_{ij}$  is the Kronecker delta, and  $P = S_{lk}\delta_{lk}$  is the local volumetric rate of expansion or contraction. Since  $S_{ij}^d\delta_{ij} = 0$  and  $\delta_{ij}n_jn_i = 1$ , we arrive at

$$S_{ij}n_jn_i = S_{ij}^d(n_jn_i - \delta_{ij}) + P/3. \quad (2.10)$$

Now we reformulate (2.9) in terms of  $P$  and of any pair of orthonormal vectors parallel to the surface,  $\mathbf{t}^1$  and  $\mathbf{t}^2$ ,

$$\vartheta = \sigma(t_k^1 S_{kj}^d t_j^1 + t_k^2 S_{kj}^d t_j^2) - \sigma P/3, \quad (2.11)$$

where we have considered that,  $n_jn_i - \delta_{ij} = -t_i^1 t_j^1 - t_i^2 t_j^2$ . The first term represents the growth rate of an infinitesimal surface area,  $\delta A$ , due to the deviatoric part of the rate-of-strain tensor, which reads

$$\frac{1}{\delta A} d_t \delta A = t_k^1 S_{kj}^d t_j^1 + t_k^2 S_{kj}^d t_j^2. \quad (2.12)$$

The second term is related to compressibility effects, and is proportional to the growth rate of an infinitesimal volume at the surface.

In the case of an incompressible flow, in which  $P = 0$  and  $S_{ij} = S_{ij}^d$ ,

$$\vartheta = \sigma(t_k^1 S_{kj} t_j^1 + t_k^2 S_{kj} t_j^2), \quad (2.13)$$

which shows that the surface energy increases as a consequence of the stretching of the surface area by the rate-of-strain tensor. The opposite mechanism is also possible, and the decrements of the surface energy are related to the contraction of the surface area. In figure 1(a,b) we show a schematic representation of these mechanisms for an incompressible flow. Hereafter, we limit our analysis to incompressible flows.

By taking volume and surface averages of (2.7), we obtain an equation for the evolution of the total kinetic energy and the total surface energy,  $\mathcal{E} = \langle e \rangle_V$  and  $\mathcal{H} = \langle h \rangle_V$ ,

$$d_t \mathcal{H} = \kappa \langle \phi \partial_{kk} \phi \rangle_V + \langle \vartheta \rangle_S, \quad (2.14)$$

$$d_t \mathcal{E} = 2 \langle \mu S_{ij} S_{ij} \rangle_V - \langle \vartheta \rangle_S + \langle u_i f_i \rangle_V, \quad (2.15)$$

where  $\langle \cdot \rangle_S$  denotes the integral over the fluid-fluid surface. On average,  $\vartheta$  is the only term responsible for the exchange of surface and kinetic energies. We stress that these equations are valid independently of the physical properties of the fluids in the mixture. Even in the case of different viscosities, the expression for  $\vartheta$  remains valid and has equal value at both sides of the interface. In this case, the balance of tangential stresses produces a discontinuity in the rate-of-strain tensor (in the sharp-interface limit), but this discontinuity only affects the off-diagonal components of the rate-of-strain tensor in a frame fixed to the interface normal vector, which do not enter  $\vartheta$  (Dopazo *et al.* 2000).

### 3. Single-drop experiments in homogeneous isotropic turbulence

The analysis presented in the previous section is valid for any configuration of the fluid-fluid interface, or flow regime. Hereinafter we apply our analysis to the dynamics of a single drop embedded in a homogeneous and isotropic turbulent flow.

#### 3.1. Numerical method

We consider two fluids with equal density and kinematic viscosity, and integrate (2.1) in a triply periodic cubic domain of volume  $L^3 = (2\pi)^3$  by projecting the equations on

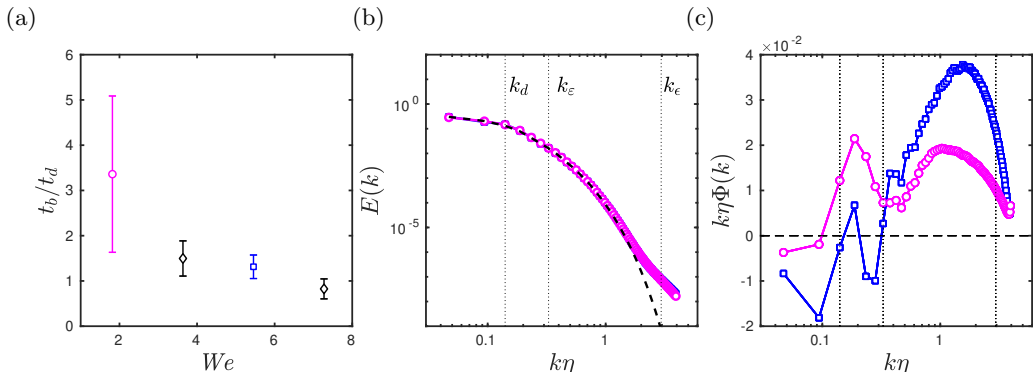


FIGURE 2. (a) Median time to breakup as a function of the  $We$ . The upper and lower bars mark plus-minus the standard deviation. (b) Kinetic energy spectra at  $Re_\lambda = 58$  for : ---, turbulent flow without droplet; —○—,  $We = 1.8$ ; —□—,  $We = 5.4$ . Vertical dotted lines mark the scale (wavenumber) of the drop,  $k_d = 2\pi/d$ , the scale where the spectral density of the kinetic energy dissipation is the highest,  $k_\varepsilon$ , and the scale of the interface,  $k_\epsilon = 2\pi/\epsilon$ . (c) Pre-multiplied production spectra,  $k\eta\Phi(k)$ . Lines as in (a). The total contribution of each wavenumber to the variation of the surface free energy is represented as the area below the curve.  $\Phi$  is normalized with its average in each case.

a basis of  $N/2$  Fourier modes in each direction, where  $N = 256$ . Non-linear terms are computed through a dealiased pseudo-spectral procedure, and a third-order semi-implicit Runge-Kutta scheme is used for the time integration, with a decomposition of the linear terms proposed by Badalassi *et al.* (2003). To sustain turbulence in a statistically steady state, we implement a linear body-force,  $\hat{f}_i = C_f \hat{u}_i$ , that is only applied to wavenumbers  $k < 2$ , where  $\hat{\cdot}$  denotes the Fourier transform and  $k$  is the wavenumber magnitude. The forcing coefficient  $C_f$  is set so that, at each time, the total kinetic energy per unit time injected in the system is constant and equal to  $\varepsilon$ , while the kinematic viscosity  $\nu = \mu/\rho$  is tuned to keep a prescribed numerical resolution,  $k_{max}\eta = 4$ , where  $\eta = (\nu/\varepsilon^4)^{3/4}$  is the Kolmogorov length scale and  $k_{max} = N/3$  is the maximum wavenumber magnitude after dealiasing.

The Reynolds number of the flow is  $Re_\lambda = \lambda u'/\nu = 58$ , where  $\lambda = \sqrt{15(\nu/\varepsilon)}u'$  is the Taylor microscale,  $u' = \sqrt{2\mathcal{E}/3}$  is the root-mean-square of the velocity fluctuations, and  $\mathcal{E} = 1/2\langle u_i u_i \rangle$  is the ensemble-averaged kinetic energy. The thickness of the fluid-fluid interface is set by the Cahn number  $Ch = (\alpha/\beta L^2)^{1/2} = 0.012$ , which for  $N = 256$  is appropriate to resolve the interface with a spectral Fourier basis (Chen & Shen 1998). The mobility  $\kappa$  defines the Peclet number,  $Pe = u' L^2 / \kappa \sqrt{\alpha\beta} = 3Ch^{-2}$ , which is fixed to ensure that the dynamics of the interface are consistent in the sharp-interface limit (Magaletti *et al.* 2013). The time-step is set to  $\Delta t = 0.04Ch$ . Simulations have been performed on GPUs using a modified version of the spectral code described in Cardesa *et al.* (2017). The code has been validated against Shao *et al.* (2018), and the consistency of the numerical parameters, such as the time-step and the spatial resolution, have been checked.

### 3.2. Initial conditions and drop size

We introduce a drop of diameter  $d = \frac{1}{3}L = 45\eta$  in a fully developed turbulent flow, and integrate the governing equations (2.1) until the drop breaks. In figure 1(c), we show a visualization of a typical single-drop simulation. Since  $d \gg \eta$ , breakup is dominated by inertial forces and characterized by the Weber number,  $We = \rho \varepsilon^{2/3} d^{5/3} / \sigma$ ,

and by a characteristic inertial time-scale  $t_d = (d^2\varepsilon)^{1/3}$ . To statistically characterise drop deformation and breakup, we perform many independent single-drop simulations initialized with statistically independent turbulent flow fields. Mass leakage (Yue *et al.* 2007) leads to a progressive reduction of the drop diameter, and to a time-dependent Weber number,  $We^\dagger(t)$ , which decreases slightly through the simulations. However, this variation is small, and therefore we do not employ any special numerical approach to prevent it (Zhang & Ye 2017; Soligo *et al.* 2019). We consider the effective Weber number of our simulations as the average Weber number at the average time of breakup,  $\langle t_b \rangle$ , i.e.  $We = \langle We^\dagger(\langle t_b \rangle) \rangle$ . The difference between the time-dependent Weber number at the time of breakup,  $We^\dagger(t_b)$ , and the effective Weber number,  $We$  is at most  $\sim 3\%$  in the worst cases.

We have performed simulations at four different effective  $We$  in the range of 1.8 – 7.4. For each  $We$  the number of simulations is approximately 100, which yields a total simulation time of between  $300t_d$  and  $1500t_d$ . From each simulation, we stored sufficient full flow fields to have fully converged statistics. In figure 2(a), we show the median and the standard deviation of the time to breakup,  $t_b$ , as a function of the  $We$ . As expected, lower values of the  $We$  yield longer times to breakup.

In what follows we show that although  $d$  is comparable to the integral scale of the flow, the drop does neither modify the structure of the surrounding turbulence nor resonate with the numerical box. The drop interacts mostly with scales smaller than  $d$ , indicating that the linear forcing used to sustain turbulence does not affect breakup. In figure 2(b), we show the average kinetic energy spectrum,  $E(k) = 2\pi k^2 \langle \hat{u} \hat{u}^* \rangle_k$ , with and without an immersed drop. Here  $\langle \cdot \rangle_k$  denotes averaging over modes with wavenumber magnitude  $k$ , and  $\cdot^*$  represents the complex conjugate. The energy spectra is similar for the flow with and without droplet above  $k\eta \sim 1$ , indicating a physical turbulent structure in those scales. To further corroborate this, we calculate the skewness and flatness factor of the longitudinal velocity derivatives,

$$\mathcal{F}_n = \frac{\langle (\partial_i u_i)^n \rangle}{\langle (\partial_i u_i)^2 \rangle^{n/2}}, \quad (3.1)$$

where no summation is intended for repeated indices. We find that, away from the drop surface,  $\mathcal{F}_3 \approx -0.52$  and  $\mathcal{F}_4 \approx 5.2$  independently of the Weber number, which are similar to the values for a simulation without the drop and in the expected range for the  $Re_\lambda$  considered (Jiménez *et al.* 1993).

The good collapse of the energy spectra in the small wavenumbers (large scales) also suggests the absence of any resonances between the drop and the box, which could lead to spurious large-scale dynamics. To examine how the large-scale forcing affects the dynamics of breakup, we study the pre-multiplied production spectra,  $k\eta\Phi(k)$ , shown in figure 2(c), where

$$\Phi(k) = -4\pi k^2 \Re \langle \widehat{(u_j \partial_j c)} \hat{\phi}^* \rangle_k, \quad (3.2)$$

describes the contribution of each scale to the changes of the surface energy due to the deformation of the interface by the velocity field. Variations of the surface energy are due mostly to turbulent fluctuations at scales below the drop diameter, whereas the contribution of larger scales is comparatively small. In fact, the contribution of the scales affected by the forcing (with  $k < 2$ ) to the production of surface energy is slightly negative on average, confirming that the forcing does not contribute to deformation and breakup.

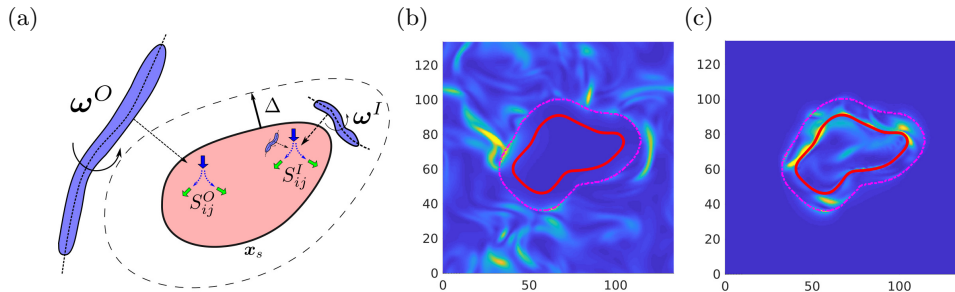


FIGURE 3. (a) Decomposition of the rate-of-strain tensor acting on the drop surface in contributions due to eddies a distance  $\Delta$  from the drop surface, denoted as  $S_{ij}^O$ , and a distance  $\Delta$  closer to the surface and inside the drop, denoted as  $S_{ij}^I$ .  $\mathbf{x}_s$  marks the drop surface. (b,c) Magnitude of the (b) inner and (c) outer rate-of-strain tensor,  $2S_{ij}^I S_{ij}^I$  and  $2S_{ij}^O S_{ij}^O$ , in a direct numerical simulation for  $\Delta = 9\eta$  and  $We = 5.4$ . The solid red line marks the drop surface, and the dashed magenta line a distance  $\Delta = 9\eta$  from the surface. Axis in Kolmogorov units.

## 4. Analysis of the energetic exchange in isotropic turbulence

### 4.1. Local and non-local surface stretching

Despite the simplicity of the energetic exchange described in §2, the coupling between the dynamics of the drop surface and the surrounding turbulence is bidirectional and highly non-linear. The rate-of-strain tensor generates surface contraction or expansion, and, at the same time, the surface dynamics generates straining motions. For instance, as a deformed drop relaxes toward a spherical shape, the surface energy follows damped oscillations before settling into equilibrium. Although these changes of the surface energy are produced by the stretching and compression of the surface, they are drop-induced and not necessarily related to drop breakup.

To separate the dynamics of the interface from the action of the surrounding turbulence, we split the surface-stretching term into contributions related to eddies close to, and inside the drop, and far from the drop. Here we consider eddies as patches of swirling fluid, and associate them with the vorticity field. The kinematic relations that hold between the vorticity vector and the rate-of-strain tensor imply that eddies away from the drop stretch its surface by non-local effects (Ohkitani & Kishiba 1995; Hamlington *et al.* 2008). We define the vorticity field at a distance  $\Delta$  from the drop surface as

$$\boldsymbol{\omega}'^O = G(\mathbf{x}; \Delta) \boldsymbol{\omega}, \quad (4.1)$$

where  $\boldsymbol{\omega} = \nabla \times \mathbf{u}$  is the vorticity vector, and

$$\begin{aligned} G(\mathbf{x}; \Delta) &= 1 \text{ if } |\mathbf{x} - \mathbf{x}_s|_s > \Delta \text{ and } \mathbf{x} \in \mathcal{O}, \\ G(\mathbf{x}; \Delta) &= 0 \text{ if otherwise,} \end{aligned} \quad (4.2)$$

is a kernel that defines the region a distance  $\Delta$  from the drop surface. Here  $\mathbf{x}_s$  defines the surface of the drop,  $|\mathbf{x} - \mathbf{x}_s|_s$  is the shortest Euclidean distance from  $\mathbf{x}$  to the drop surface, and  $\mathcal{O}$  comprises all the points outside the drop. Let us note that  $\boldsymbol{\omega}'^O$  does not define a vorticity field because it does not, in general, fulfill that  $\nabla \cdot \boldsymbol{\omega}'^O = 0$ . We thus project it into the closest divergence-free field,  $\boldsymbol{\omega}^O = \boldsymbol{\omega}'^O - \nabla \psi$ , by solving

$$\nabla^2 \psi = \nabla \cdot \boldsymbol{\omega}'^O, \quad (4.3)$$

with periodic boundary conditions. The stretching induced on the drop by the eddies away from its surface can be calculated from the Biot–Savart law. By taking the curl of

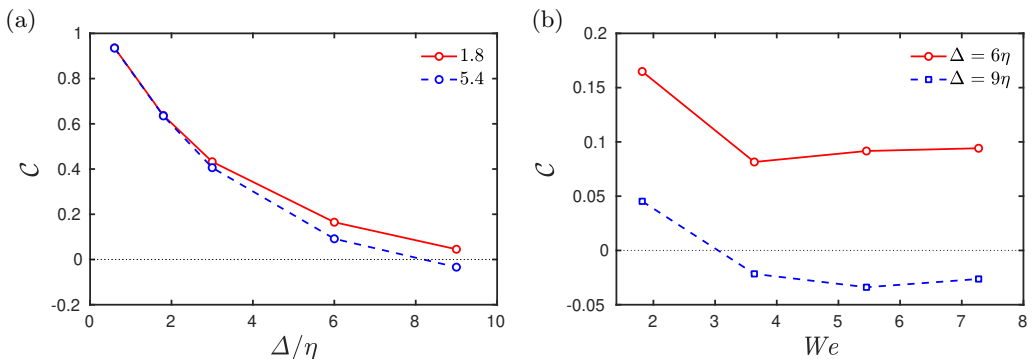


FIGURE 4. (a,b) Correlation coefficient  $\mathcal{C}$  between  $\vartheta^I$  and  $\vartheta^O$  as a function of (a)  $\Delta$  and (b)  $We$ .

the vorticity and considering that  $\nabla \cdot \mathbf{u}^O = 0$ , we obtain the following equation

$$\nabla^2 \mathbf{u}^O = -\nabla \times \boldsymbol{\omega}^O, \quad (4.4)$$

which, when solved with periodic boundary conditions, provides the rate-of-strain tensor induced on the surface of the drop by eddies further and closer than  $\Delta$  from the drop surface,  $S_{ij}^O = \frac{1}{2}(\partial_j u_i^O + \partial_i u_j^O)$  and  $S_{ij}^I = S_{ij} - S_{ij}^O$ .

The stretching of the drop surface by eddies at distances larger than  $\Delta$  from the drop surface is  $\vartheta^O = -n_i S_{ij}^O n_j$ , where the rate-of-strain tensor is evaluated at the surface of the drop, whereas  $\vartheta^I = -n_i S_{ij}^I n_j$  is the stretching induced on the surface by the flow field inside the drop and at a distance smaller than  $\Delta$  from the drop surface. A schematic representation of this decomposition and its application to a direct numerical simulation are shown in figures 3(a)–(c).

#### 4.2. Stretching by inner and outer eddies

We use here the decomposition presented in the previous section to separate the total surface stretching into two contribution. First, a contribution due to eddies close to the drop surface (or inside the surface) which are affected by surface dynamics or by the material properties of the drop, and, second, another due to eddies far from the surface, which are not affected by surface dynamics and independent of the material properties of the drop. We call them ‘inner’ and ‘outer’ eddies respectively. In this section, we show that in fact a separation in surface-driven, or ‘inner’, and surface-independent, or ‘outer’, eddies takes place at a small distances (compared to the drop diameter) from the drop surface.

A practical formal definition of the limit that separates inner and outer eddies is the smallest  $\Delta$  for which the outer stretching is independent of surface dynamics, i.e when there is not a coupled interaction between outer eddies and the surface. This definition identifies the smallest region close to the drop surface affected by surface dynamics.

Since, as we will show in the following sections,  $\vartheta^I$  is strongly influenced by surface dynamics, we use the correlation coefficient between  $\vartheta^O$  with  $\vartheta^I$  evaluated at the drop surface to quantify the independence of ‘outer’ eddies. The correlation coefficient is defined as

$$\mathcal{C} = \frac{\langle \overline{\vartheta^I} \cdot \overline{\vartheta^O} \rangle}{\sqrt{\langle \overline{\vartheta^{I^2}} \rangle \langle \overline{\vartheta^{O^2}} \rangle}}, \quad (4.5)$$

where the bar denotes quantities without their average. We measure  $\mathcal{C}$  for different  $We$

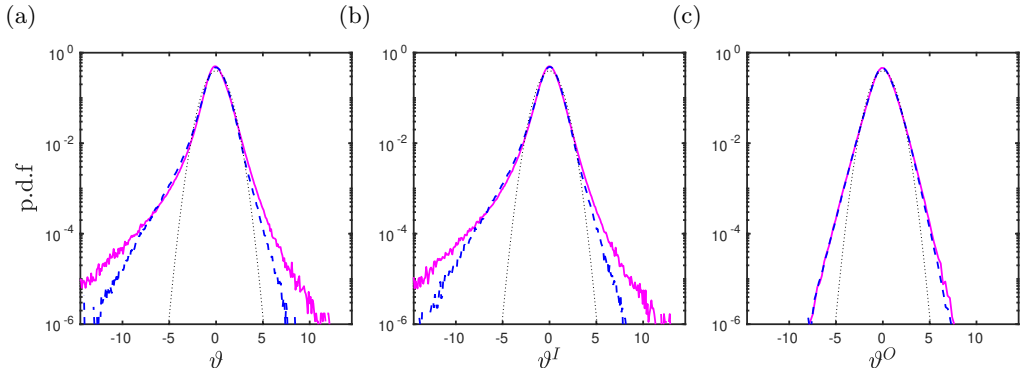


FIGURE 5. Probability density function of the local surface stretching due to (a) the full flow,  $\vartheta$ , (b) the inner eddies,  $\vartheta^I$ , and (c) the outer eddies,  $\vartheta^O$ , for  $\Delta = 6\eta$  and at  $We =$ : —, 1.8; ---, 5.4. Quantities plotted without the mean and divided by their standard deviation.

and  $\Delta$ , and present the results in figures 4(a,b). The correlation coefficient is close to unity for  $\Delta \sim 0$ , and decays fast with increasing  $\Delta$ . For  $\Delta = 6\eta$ ,  $\mathcal{C} \approx 0.2$ , and for  $\Delta = 9\eta$  it drops close to zero. As  $We$  decreases, the correlation coefficient increases slightly, suggesting that the effect of surface dynamics on the surrounding eddies increases with surface tension. These results suggest that  $\Delta$  between  $6\eta = 0.12d$  and  $9\eta = 0.19d$  is a good approximation of the limit that separates ‘outer’ and ‘inner’ eddies, and that this limit does not change substantially in the range of  $We$  considered here.

#### 4.3. Statistics of the surface stretching

In figure 5(a)–(c), we show the probability density function (p.d.f) of  $\vartheta$ ,  $\vartheta^O$ , and  $\vartheta^I$  measured at the surface of the drop for  $We = 1.8$  and  $5.4$ , and for  $\Delta = 6\eta = 0.13d$ . We find that  $\vartheta$  and  $\vartheta^I$  are very similar and display fairly fat-tailed distributions which depend on the  $We$ . On the other hand, the p.d.f’s of  $\vartheta^O$  are more symmetric, closer to a Gaussian. The good collapse of the pdf’s at two different  $We$  suggests that the surface stretching produced by eddies a distance further than  $\Delta = 6\eta = 0.13d$  from the drop is not affected by surface dynamics. These results are qualitatively similar for  $\Delta = 9\eta = 0.19d$ .

In figure 6(a), we show the mean of  $\vartheta$ ,  $\vartheta^O$ , and  $\vartheta^I$  normalised with  $\rho u_d^3$ , where  $u_d = d/t_d$ , for different values of  $We$  and  $\Delta$ . The average of  $\vartheta$  increases with  $We$ , which is consistent with the statistics of the breakup time. Assuming that the breakup of an initially spherical drop takes place when a critical increment of the surface energy is reached,  $\Delta\mathcal{H}_b$  (Andersson & Andersson 2006), and that the surface energy can only increase due to the stretching term, its average measured on the surface of the drop is related to the time to breakup by

$$t_b \sim \left\langle \frac{\Delta\mathcal{H}_b}{\vartheta d^2} \right\rangle, \quad (4.6)$$

which has been estimated by averaging equation (2.14) in time, considering that  $\langle \vartheta \rangle_S \sim \langle \vartheta \rangle d^2$ , and neglecting the dissipation of surface energy. As  $We$  decreases, the time to breakup increases (figure 2(a)), and  $\langle \vartheta \rangle$  decreases.

For  $\Delta = 6\eta$  and  $\Delta = 9\eta$ , the average contribution of the outer eddies to the stretching of the interface is larger than, or at least comparable to, the inner contribution, and this contribution changes only slightly with the  $We$ . Conversely, the inner contribution increases substantially with  $We$ , transitioning from  $\langle \vartheta^I \rangle < 0$  at low  $We$  to  $\langle \vartheta^I \rangle > 0$  at

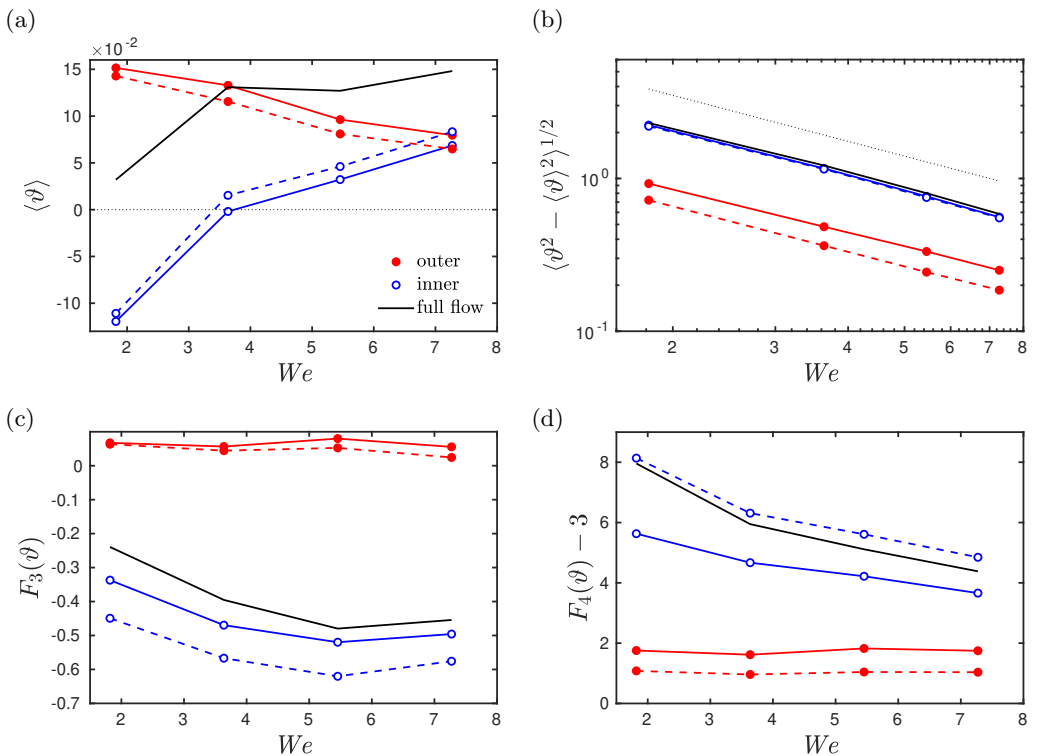


FIGURE 6. (a) Mean, (b) standard deviation, (c) skewness and (d) excess flatness of  $\vartheta$  as a function of  $We$ . Mean and standard deviation normalized with  $\rho u_d^3$ , where  $u_d = d/t_d$ . Solid symbols corresponds to the statistics of  $\vartheta^O$ , and empty symbols to  $\vartheta^I$ . Color lines correspond to  $\Delta =$ : —,  $6\eta$ ; ---,  $9\eta$ ; and solid black line to the full rate-of-strain tensor. In (b) the dotted line is proportional to  $We^{-1}$ .

high  $We$ . This transition takes place at approximately  $We \sim 3.5$ , and will be examined in §4.5.

In figure 6(b), we show the standard deviation of  $\vartheta$  normalised with  $\rho u_d^3$ . It is approximately proportional to  $We^{-1}$ , and substantially higher for the inner than for the outer contributions. In all cases, the standard deviation of the local surface stretching is larger than its mean, and this difference becomes particularly significant as  $We$  decreases. These results suggest that a very significant part of the stretching is not efficient, and cancels out when averaging, specially for the inner stretching and for small Weber numbers.

We focus now on higher order statistics of the surface stretching, in particular in the skewness and the flatness factor, which are defined as

$$F_n(\vartheta) = \langle (\vartheta - \langle \vartheta \rangle)^n \rangle / \langle \vartheta^2 - \langle \vartheta \rangle^2 \rangle^{n/2}, \quad (4.7)$$

for  $n = 3$ , and  $n = 4$  respectively, and are shown in in figures 6(c,d). For ease of reference, we consider the so-called excess flatness factor, i.e the flatness factor minus that of a Gaussian distribution, for which  $F_4 = 3$ . These statistical moments emphasize the strong distinction between inner and outer stretching. While the skewness of the outer contributions is close to zero and does not change with  $We$ , the statistics of the inner stretching are more negatively skewed, and show dependence with  $We$ . The flatness factor conveys a similar picture. The outer contributions have a low,  $We$ -independent, flatness factor, whereas for the inner contributions the flatness factor increases substantially with

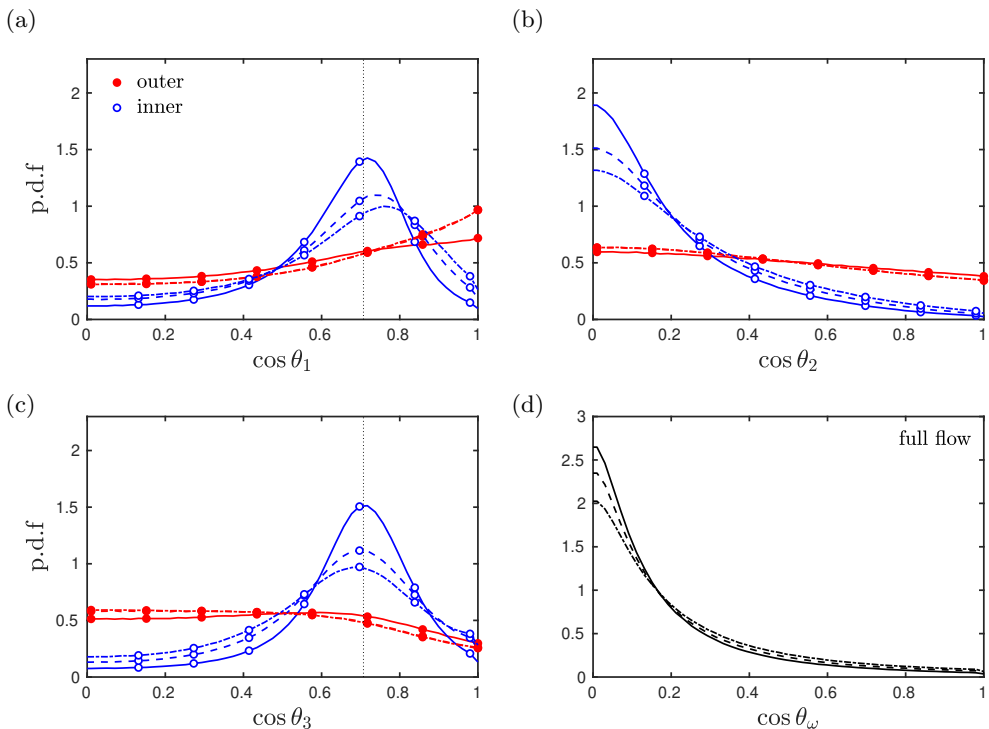


FIGURE 7. (a)-(c) Probability density function of  $\cos \theta_i = \mathbf{n} \cdot \mathbf{v}_i$ , where  $\mathbf{v}_i$  are the principal directions of the rate of strain tensor and  $\lambda_1 \leq \lambda_2 \leq \lambda_3$  are their eigenvalues. Solid markers correspond to angles calculated with the inner flow field, and empty markers to the outer field for  $\Delta = 9\eta$ . (d) Similar but for the vorticity vector of the full flow field,  $\cos \theta_\omega = \mathbf{n} \cdot \boldsymbol{\omega}/|\boldsymbol{\omega}|$ . Lines correspond to  $We =$ : —, 1.8; ---, 3.6; - · -, 5.4. The vertical dotted line in (a) and (c) marks  $\cos \pi/4$ .

decreasing  $We$ . These results corroborate, first, that the statistics of the outer stretching are roughly  $We$ -independent, as anticipated by the remarkable collapse in figure 5(c), and, second, that the inner stretching has an intermittent structure, with intense events of  $\vartheta$  becoming stronger with decreasing  $We$ .

#### 4.4. Geometrical characterization of the inner and outer stretching

To further explain the statistical differences between the inner and outer contributions, and their dependence with  $We$ , we study the structure of the rate-of-strain tensor induced by inner and outer eddies, and of the vorticity vector, on the surface of the drop. In the spirit of the analysis of vortex stretching in isotropic turbulence (Ashurst *et al.* 1987), we analyse the surface stretching term in the frame of reference of the eigenvectors of the rate-of-strain tensor, and quantify the contribution of each of its eigenvalues to the total stretching of the drop surface.

In figure 7(a)-(c), we show the p.d.f of the cosine of the angle of alignment between each of the principal axes of the rate of strain tensor,  $\mathbf{v}_1$ ,  $\mathbf{v}_2$  and  $\mathbf{v}_3$  (where  $\lambda_1 \leq \lambda_2 \leq \lambda_3$  are their corresponding eigenvalues) and the normal to the surface,  $\mathbf{n}$ . For the inner contributions, the most stretching ( $\mathbf{v}_3$ ) and the most compressing ( $\mathbf{v}_1$ ) eigenvectors tend to be oriented at  $\sim 45^\circ$  with respect to the surface normal, and therefore also to the surface tangent plane, while the intermediate eigenvalue is predominantly normal to the surface normal (parallel to the surface tangent plane). As shown in figure 7(d), also the

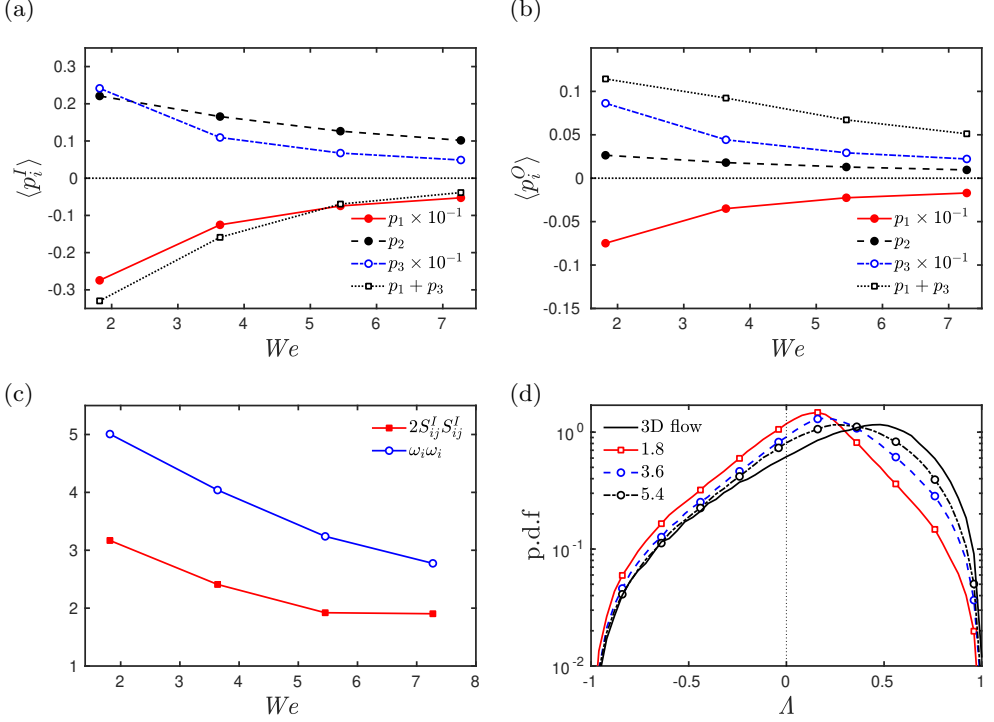


FIGURE 8. (a,b) Average surface stretching due to each eigenvalue of the rate-of-strain tensor,  $p_i = \sigma \lambda_i \sin^2 \theta_i$  as a function of the Weber number for the inner (a) and the outer (b) contributions, for  $\Delta = 9\eta$ . Surface stretching normalised with  $\rho u_d^3$ . (c) Surface average of the square of the inner rate-of-strain tensor,  $2S_{ij}^I S_{ij}^I$ , for  $\Delta = 9\eta$ , and the vorticity vector  $\omega_i \omega_i$  for different Weber numbers, normalised with Kolmogorov units. (d) p.d.f of  $\Lambda = \log_2 |\lambda_1|/\lambda_3$  for different Weber numbers.

vorticity vector aligns strongly normal to  $\mathbf{n}$ , and parallel to the surface. This tendency was also reported by Soligo *et al.* (2020). In all cases, the alignment is more marked for small  $We$ , revealing an important effect of surface dynamics on the configuration of the velocity gradients at the surface.

The outer contributions to the stretching of the surface show a substantially different picture. There is a consistent tendency of the most compressing eigenvector to align normal to the surface, and of the most stretching to align parallel to it, although the alignment is less marked than for the inner rate-of-strain tensor. The good collapse at different  $We$  suggests that this effect is roughly independent of the surface dynamics.

We further decompose the surface stretching term into the contribution of each of its eigenvalues. A possible approach is to consider the rate of compression or stretching of the vector normal to the surface by each eigenvalue,  $r_i = -\sigma \lambda_i \sin \theta_i$  (no summation for repeated indices is intended), which yields

$$\vartheta = r_1 + r_2 + r_3 = -\sigma(\lambda_1 \cos^2 \theta_1 + \lambda_2 \cos^2 \theta_2 + \lambda_3 \cos^2 \theta_3). \quad (4.8)$$

However this decomposition cannot be readily interpreted from a physical perspective. Instead, we consider the contribution of each eigenvalue to the stretching or compression of the surface tangent plane,  $p_i = \sigma \lambda_i \sin^2 \theta_i$ . Note that  $\sin \theta_i = \cos(\pi/2 - \theta_i)$  is the projection of each eigenvector on the surface tangent plane. Since  $\lambda_1 + \lambda_2 + \lambda_3 = 0$ , and

$\cos^2 \theta_i = 1 - \sin^2 \theta_i$ , the total surface stretching reads,

$$\vartheta = p_1 + p_2 + p_3 = \sigma(\lambda_1 \sin^2 \theta_1 + \lambda_2 \sin^2 \theta_2 + \lambda_3 \sin^2 \theta_3). \quad (4.9)$$

In figures 8(a,b), we show the averages of  $p_i$  for the inner and outer contributions. In both cases the surface stretching and compression due to  $p_1$  and  $p_3$  is much larger in absolute value than that of  $p_2$  (note that in the plot  $p_1$  and  $p_3$  are divided by 10 for ease of visualization). However, there is a significant cancellation between  $p_1$  and  $p_3$ , so that  $\langle p_1 + p_3 \rangle \sim \langle p_2 \rangle$ .

For the outer contribution,  $p_1 + p_3$  produces net surface stretching, which can be traced to the tendency of  $\mathbf{v}_3$  to align parallel to the surface (or  $\mathbf{v}_1$  normal to it), and  $p_2$  does not play a relevant role in the average stretching. This is in agreement with the almost random orientation of  $\mathbf{v}_2$  with respect to the surface normal, as shown in figure 7(b).

For the inner contributions, the cancellation of  $p_1$  and  $p_3$  is consistent with a predominant alignment of  $\mathbf{v}_1$  and  $\mathbf{v}_3$  at  $\sim 45^\circ$  with respect to the normal and to the surface tangent plane. In this case,  $p_2$  contributes substantially to the average stretching of the surface. As  $We$  increases, the absolute value of  $\langle p_1 + p_3 \rangle$  decreases, and  $\langle p_2 \rangle$  progressively dominates the average stretching, explaining the transition from  $\langle \vartheta^I \rangle < 0$  to  $\langle \vartheta^I \rangle > 0$  as  $We$  increases.

#### 4.5. Transition from a 2D to a 3D structure of the rate-of-strain tensor

We focus now on the intensity and structure of the velocity gradients at the drop surface. In figure 8(c), we show the average of  $2S_{ij}^I S_{ij}^I$  for  $\Delta = 9\eta$ , and  $\omega_i \omega_i$ , measured at the surface of the drop. Although the surface dynamics increases the intensity of the velocity gradients on the surface of the drop with decreasing  $We$ , surface tension forces impose a strong constraint on their structure. The constraint of the velocity gradients is very noticeable in the rate-of-strain tensor, which has a quasi-2D structure at low  $We$ , with  $|\lambda_2| \ll |\lambda_3| \approx |\lambda_1|$ , and becomes progressively 3D as  $We$  increases. To characterise this process we analyse

$$\Lambda = \log_2 \frac{|\lambda_1|}{\lambda_3}, \quad (4.10)$$

at the drop surface. Since  $\frac{1}{2}\lambda_3 \leq |\lambda_1| \leq 2\lambda_3$ , this quantity is defined in the range  $-1 \leq \Lambda \leq 1$ . Predominant  $\Lambda > 0$  is characteristic of fully developed 3D turbulence, and implies that  $\lambda_2 > 0$  on average, while  $\Lambda = 0$  indicates 2D dynamics, in which  $\lambda_1 = -\lambda_3$  and, by continuity,  $\lambda_2 = -\lambda_1 - \lambda_3 = 0$ . As shown in figure 8(d), the p.d.f of  $\Lambda$  shows that, for small  $We$ ,  $|\lambda_1| \sim \lambda_3$  and  $\lambda_2 \sim 0$ , and that, on average,  $\lambda_2$  grows positive as  $We$  increases, indicating a transition from a quasi-2D to a 3D structure of the rate-of-strain tensor at the surface. As  $\lambda_2$  increases with respect to  $\lambda_3$  and  $|\lambda_1|$ , the net stretching that it produces on the surface becomes more relevant, and, as shown in the previous section,  $\langle p_2 \rangle$  dominates over  $\langle p_1 + p_3 \rangle$ , leading to  $\langle \vartheta^I \rangle > 0$ .

## 5. Discussion

We have separated the total stretching of the drop surface in contributions from inner and outer eddies. For distances to the drop surface larger than  $\Delta > 6\eta$ , the two contributions are not correlated pointwise (figure 4), indicating that outer eddies are independent of surface dynamics. This is corroborated by the statistics of the outer surface stretching, which are roughly  $We$ -independent. The surface stretching due to outer eddies contributes on average to the increment of the surface energy at all  $We$ , and

its statistics do not depend strongly on  $We$ , which implies that they depend mostly on the structure of the surrounding turbulence.

For low  $We$ , the surface dynamics produces a net energy flux from the surface energy to turbulent kinetic energy, while for large  $We$ , the inner eddies tend to stretch the surface on average, increasing the surface energy. In all cases, the inner surface stretching term shows strongly intermittent and negatively-skewed  $We$ -dependent statistics. Intense negative events of the surface stretching become more relevant as  $We$  decreases, evidencing the enhanced ability of the surface to restore the deformations caused by turbulent fluctuation, and transferring the surface energy back to turbulent fluctuations. By conservation, this energy is on average dissipated by the flow. In this low- $We$  scenario, the net increments of the total surface energy depend on the interplay between outer surface stretching and the ability of the surface to transfer energy through inner eddies into turbulent fluctuations.

By analysing the structure of the inner velocity gradients on the surface of the drop, we have shown that at low  $We$  the rate-of-strain tensor is strongly controlled by surface tension forces. Although its average magnitude is larger than in the turbulent background, providing enhanced dissipation of turbulent kinetic energy, its 2D structure and its configuration with respect to the interface precludes the net stretching of the surface. As  $We$  increases and surface tension forces become less dominant, the rate-of-strain tensor develops a 3D structure in which its intermediate eigenvalue becomes predominantly positive, producing net stretching of the surface. This phenomenon explains the transition from a negative to a positive average contribution of the inner eddies to the total surface stretching.

We have reported a statistically significant alignment of the surface normal with the most compressing direction of the outer rate-of-strain tensor, and of the surface tangent plane with the most stretching one. This phenomenon, which is also observed in the evolution of passive material surfaces in turbulence, and naturally leads to this configuration (Girimaji & Pope 1990), indicates the persistent stretching of the drop surface by outer eddies. The similar statistics of the alignment angles in a wide range of  $We$  suggests that this mechanism is rather independent of surface dynamics. The stretching by outer eddies is a plausible mechanism for drop deformation, with the exception that the drop surface interacts with the fluid, and resists deformation.

## 6. Conclusions

In this work we have analysed the energetics of fluid-fluid interfaces. Our main contribution is to provide a mathematical description of the mechanism responsible for the energetic exchange between the kinetic energy of the flow and the surface energy of the fluid-fluid interface. We have shown that this exchange occurs due to the stretching or compression of the surface area by the rate-of-strain tensor. There result stress the relevant role of straining motions in drop deformation and breakup, in agreement with experiments and theoretical analyses of laminar flows in the Stokes limit (Rallison 1984).

We have separated the total stretching into contributions due to inner and outer eddies. We use here the term outer to refer to eddies sufficiently far from the drop surface for their dynamics to be unaffected by surface tension forces. Conversely, we define inner eddies as those close to the surface or inside the drop, whose dynamics are affected either by surface tension forces or by the material properties of the fluid inside the drop. The stretching of the drop surface by outer eddies contributes substantially to the total surface energy budget. This mechanism constitutes a quantitative reinterpretation of the ‘collision’ of eddies (Andersson & Andersson 2006).

We have shown that the surface stretching due to inner and outer eddies are locally uncorrelated, indicating that these terms may be considered separately. A ‘random’ approach to breakup modelling appears to be justified since outer eddies are, by definition, not coupled to the dynamics of the interface, precluding any synergies that may lead to enhanced breakup (at least in the simple case of equal density and viscosity). An interesting question is how this analysis applies to bubbles, for which their characteristic oscillatory frequency seems to play a relevant role in breakup (Risso & Fabre 1998). In drops, deformation and breakup necessarily occurs as an interplay between inner and outer dynamics, but we suggest that the latter may be the driver of the process. In the context of drop deformation and breakup, our results pave the way for a better understanding of this phenomenon from an energetic perspective, and provide a consistent quantitative framework to tune, improve and develop breakup models.

Although our study is limited to the ideal case of incompressible fluids with equal density and viscosity, the theoretical analysis in §4 applies equally to compressible fluids, and to fluid pairs with different viscosity and density. In the latter case, we expect the contribution of inner dynamics to change considerably. For instance, we suggest that an increment of the drop viscosity substantially affects the inner dynamics due, first, to the kinematic relations imposed on the rate-of-strain tensor across the interface, which depend on the viscosity ratio (Dopazo *et al.* 2000), and second, by the enhanced ability of the fluid inside the drop to diffuse momentum and dissipate energy. These changes may inhibit the stretching of the surface by inner eddies and/or provide a fast mechanism to dissipate the surface energy produced by the stretching of outer eddies, explaining the resistance of viscous drops to breakup (Calabrese *et al.* 1986; Roccon *et al.* 2017).

An important question that we have partially addressed in this work is whether breakup occurs as a progressive buildup of surface energy due to the accumulative interaction with many eddies, or as sharp increments of the surface energy due to interaction with isolated intense turbulent events. Although answering this question necessarily requires temporal analysis, we have shown that the standard deviation of the local surface stretching is much larger than its mean, possibly reflecting inefficient stretching that cancels out. These results point in the direction of the second scenario. A tentative picture is that weak background turbulence produces much of this inefficient stretching, whereas the interaction with just a few of the most intense turbulent structures produces the effective stretching leading to breakup.

## Acknowledgements

A.V-M acknowledges the support of the European Research Council COTURB project ERC-2014.AdG-669505.

## Declaration of interest

The authors report no conflict of interest.

## REFERENCES

- AIYER, A.K., YANG, D., CHAMECKI, M. & MENEVEAU, C. 2019 A population balance model for large eddy simulation of polydisperse droplet evolution. *J. Fluid Mech.* **878**, 700–739.
- ANDERSSON, R. & ANDERSSON, B. 2006 On the breakup of fluid particles in turbulent flows. *AIChE Journal* **52**, 2020–2030.
- ASHURST, W.T., KERSTEIN, A.R., KERR, R.M. & GIBSON, C.H. 1987 Alignment of vorticity

- and scalar gradient with strain rate in simulated navier–stokes turbulence. *Phys. Fluids* **30**, 2343–2353.
- BADALASSI, V.E., CENICEROS, H.D. & BANERJEE, S. 2003 Computation of multiphase systems with phase field models. *J. Comput. Phys.* **190**, 371–397.
- CALABRESE, R.V., CHANG, T.P.K. & DANG, P.T. 1986 Drop breakup in turbulent stirred-tank contactors. Part I: Effect of dispersed-phase viscosity. *AIChE J.* **32**, 657–666.
- CARDESA, J.I., VELA-MARTÍN, A. & JIMÉNEZ, J. 2017 The turbulent cascade in five dimensions. *Science* **357**, 782–784.
- CHEN, L.Q. & SHEN, J. 1998 Applications of semi-implicit fourier-spectral method to phase field equations. *Comput. Phys. Commun.* **108**, 147–158.
- DODD, M.S. & FERRANTE, A. 2016 On the interaction of taylor length scale size droplets and isotropic turbulence. *J. Fluid Mech.* **806**, 356–412.
- DOPAZO, C., LOZANO, A. & BARRERAS, F. 2000 Vorticity constraints on a fluid/fluid interface. *Phys. Fluids* **12**, 1928–1931.
- EASTWOOD, C.D., ARMI, L. & LASHERAS, J.C. 2004 The breakup of immiscible fluids in turbulent flows. *J. Fluid Mech.* **502**, 309–333.
- GIRIMAJI, S.S. & POPE, S.B. 1990 Material-element deformation in isotropic turbulence. *J. Fluid Mech.* **220**, 427–458.
- HAKANSSON, A. 2019 Emulsion formation by homogenization: Current understanding and future perspectives. *Annu. Rev. Food Sci. Technol.* **10**, 239–258.
- HAMLINGTON, P.E., SCHUMACHER, J. & DAHM, W.J.A. 2008 Local and nonlocal strain rate fields and vorticity alignment in turbulent flows. *Phys. Rev. E* **77** (2), 026303.
- HINZE, J.O. 1955 Fundamentals of the hydrodynamic mechanism of splitting in dispersion processes. *AIChE Journal* **1** (3), 289–295.
- JACQMIN, D. 1999 Calculation of two-phase Navier–Stokes flows using phase-field modeling. *J. Comput. Phys.* **155**, 96–127.
- JIMÉNEZ, J., WRAY, A., SAFFMAN, P.G. & RO GALLO, R.S. 1993 The structure of intense vorticity in isotropic turbulence. *J. Fluid Mech.* **255**, 65–90.
- KOLMOGOROV, A.N. 1949 On the disintegration of drops in turbulent flow. In *Doklady Akad. Nauk. USSR*, , vol. 66, p. 825.
- LASHERAS, J.C., EASTWOOD, C., MARTINEZ-BAZÁN, C. & MONTANES, J.L. 2002 A review of statistical models for the break-up of an immiscible fluid immersed into a fully developed turbulent flow. *Int. J. Multiph. Flow* **28**, 247–278.
- LIAO, Y. & LUCAS, D. 2009 A literature review of theoretical models for drop and bubble breakup in turbulent dispersions. *Chem. Eng. Sci.* **64**, 3389–3406.
- MAASS S. & KRAUME, M. 2012 Determination of breakage rates using single drop experiments. *Chem. Eng. Sci.* **70**, 146 – 164.
- MAGALETTI, F., PICANO, F., CHINAPPI, M., MARINO, L. & CASCIOLA, C. M. 2013 The sharp-interface limit of the Cahn–Hilliard/Navier–Stokes model for binary fluids. *J. Fluid Mech.* **714**, 95–126.
- OHKITANI, K. & KISHIBA, S. 1995 Nonlocal nature of vortex stretching in an inviscid fluid. *Phys. Fluids* **7**, 411–421.
- RALLISON, J.M. 1984 The deformation of small viscous drops and bubbles in shear flows. *Annu. Rev. Fluid Mech.* **16**, 45–66.
- RISSE, F. & FABRE, J. 1998 Oscillations and breakup of a bubble immersed in a turbulent field. *J. Fluid Mech.* **372**, 323–355.
- ROCCON, A., DE PAOLI, M., ZONTA, F. & SOLDATI, A. 2017 Viscosity-modulated breakup and coalescence of large drops in bounded turbulence. *Phys. Rev. Fluids* **2** (8), 083603.
- SHAO, CHANGXIAO, LUO, KUN, YANG, YUE & FAN, JIANREN 2018 Direct numerical simulation of droplet breakup in homogeneous isotropic turbulence: The effect of the weber number. *Int. J. Multiph. Flow* **107**, 263–274.
- SOLIGO, G., ROCCON, A. & SOLDATI, A. 2019 Mass-conservation-improved phase field methods for turbulent multiphase flow simulation. *Acta Mechanica* **230**, 683–696.
- SOLIGO, G., ROCCON, A. & SOLDATI, A. 2020 Effect of surfactant-laden droplets on turbulent flow topology. *Phys. Rev. Fluids* **5**, 073606.
- YUE, P., ZHOU, C. & FENG, J. J. 2007 Spontaneous shrinkage of drops and mass conservation in phase-field simulations. *J. Comput. Phys.* **223**, 1–9.

ZHANG, YUJIE & YE, WENJING 2017 A flux-corrected phase-field method for surface diffusion.  
*Commun. Comput. Phys.* **22**, 422–440.